Electron-Based Touchless Potential Sensing of Shape Primitives and Differentially-Charged Spacecraft

Miles T. Bengtson* and Hanspeter Schaub[†]
University of Colorado Boulder, Boulder, Colorado 80303

Numerous missions are being proposed which involve multiple spacecraft operating in close proximity in harsh charging environments. In such missions, the ability to sense the electrostatic potential on a nearby object is critical to prevent harmful electrostatic discharges or to leverage Coulomb interactions for relative motion control. The electron method is one such technique for touchless potential measurement which works by measuring low-energy secondary or photoelectrons emitted from the target. Previous work has demonstrated the efficacy of the electron method for touchless sensing, but has been limited to consideration of simple shapes and uniformly charged targets. This paper investigates the electron method for touchless sensing for cases in which the target spacecraft has more complex geometry primitives, including boxes, panels, and dishes. Further, the differential charging case, in which the target object is charged to multiple, different potentials, is also considered. A simulation framework is developed to model electric fields and particle trajectories around such spacecraft geometries. Vacuum chamber experiments validate the simulation results. The study shows how the target geometry can focus or defocus the electron flux into streams of electrons emanating from the surface. This provides critical insight into where to place the servicer vehicle to measure these fluxes and determine the target spacecraft potential.

Nomenclature

A	=	area, m^2
$\boldsymbol{B}$	=	magnetic field vector, T
d	=	error threshold distance, m
$\boldsymbol{E}$	=	electric field vector, $V \cdot m^{-1}$
$\boldsymbol{F}$	=	force vector acting on a charged particle, N
L	=	length of side of triangle, m
p_{xx}	=	fitting parameters
$\boldsymbol{Q}$	=	charge matrix, C
q	=	electron charge, C
$\boldsymbol{r}$	=	test point position vector, m
$\boldsymbol{S}$	=	elastance matrix, F^{-1}
t	=	time, s
$\boldsymbol{V}$	=	potential matrix, V
$\boldsymbol{v}$	=	velocity vector of charged particle, $m \cdot s^{-1}$
$\boldsymbol{x}$	=	position vector of charged particle, m
ϵ_0	=	permittivity of free space, $F \cdot m^{-1}$
σ	=	surface charge density, $C \cdot m^{-2}$

Subscript

i, j	=	iteration variables

I. Introduction

AN EMERGING challenge in the field of spacecraft charging is how to sense the voltage on an object from a distance [1]. This capability is becoming increasingly important as the geosynchronous Earth orbit (GEO) region becomes increasingly congested [2,3]. Operators are looking to conduct servicing and salvaging missions to extend lifetimes of costly assets [4–6], and debris removal missions are being proposed to free up valuable GEO slots and prevent collisions [7]. The electrostatic tractor is a concept in which Coulomb

forces between a debris object and a tractor satellite are used to touchlessly tug the debris from GEO into a graveyard orbit [8–10]. Other concepts consider using Coulomb forces and torques to remotely detumble uncontrolled objects [11] or form virtual structures consisting of several smaller spacecraft instead of a single monolithic satellite [12]. Upcoming crewed operations in cislunar space require rendezvous and docking of multiple spacecraft in environments conducive to high levels of spacecraft charging and in which a hazardous electrostatic discharge between docking craft could occur [13]. Therefore, the capability to touchlessly sense the electrostatic potential of an object from a nearby craft is an important technology for future space missions, necessary both to prevent harmful electrostatic discharges and to leverage Coulomb forces and torques for desired relative motion.

The electron method is one promising approach for touchlessly sensing the potential of nearby spacecraft. When a primary electron strikes a surface, one or more secondary electrons can be generated on the surface, depending on the energy of the primary electron. These secondary electrons have very low energies of a few electron volts. Similarly, photoelectrons are generated when a photon strikes a surface with an energy greater than the work function of the surface material. Photoelectrons are also created with initial energies of a few electron volts. If a nearby sensing craft achieves a positive potential relative to the object of interest, the secondary electrons and photo-electrons are accelerated toward the sensing craft where they can be measured. The ultimate energy of the electrons is equal to the potential difference through which they were accelerated (plus their small energy), which is the potential difference between the two craft. Therefore, if the sensing craft knows its own potential, the potential of the target object is determined. Figure 1 shows a concept figure for electron-based touchless potential sensing.
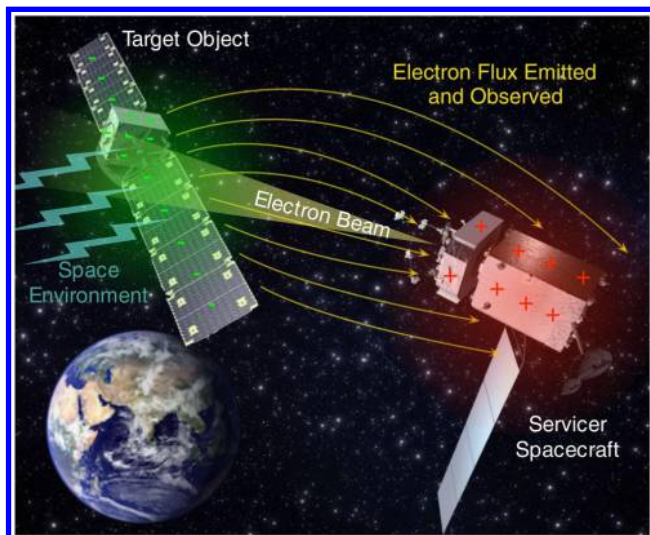
Both active and passive sensing cases are feasible. In the active case, an electron beam is directed from the sensing craft toward the target object to transfer charge and generate Coulomb forces and torques. Secondary electrons are created on the target surface by the incident electron beam and are then accelerated toward the sensing craft where they are measured to determine the forced potential of the target. In the passive case, the target surface is exposed to sunlight, which produces photoelectrons, and to the energetic electron and proton environment, which produces secondary electrons. Both the photoelectrons and secondary electrons are then accelerated away from the target surface and detected by the sensing craft to determine the natural (unforced) potential of the target.

Previous studies demonstrate both theoretically and experimentally that the electron sensing method can accurately determine the

Fig. 1 Concept figure depicting operation of the electron method for touchless electrostatic sensing. (Reproduced with permission from Bengtson et al. [14].)

potential of a target object [14,15]. However, this prior work is limited to considering simplified cases of flat plates or spheres at homogeneous potentials. In this study, the flow of low-energy electrons away from charged target objects with spacecraft shape primitives, such as boxes, panels, cylinders, and dishes, is considered. Further, electron emission from differentially charged target objects is also investigated. As with curved surfaces, the differential charging causes complex electric fields that can steer or divert the electron flux. The scope of this work is to investigate through planar electron flux studies the changes in the charge flux around such complex electric fields, and to study how this impacts the touchless charge sensing application. The paper is outlined as follows: Sec. II describes the numerical simulations and experimental facility used in this study, Sec. III analyzes the touchless sensing concept as applied to spacecraft shape primitives, and Sec. IV discusses sensing of potential on differentially charged targets. Finally, Sec. V provides a summary and conclusions.

II. Methods

A. Simulation Framework

Electrons emitted from a spacecraft are guided by the electric field, which is determined by the geometry and charge distribution of that spacecraft. Therefore, the shape and charge distribution of the target object play an important role in the sensing process. It is a well-known result that the electric field at the surface of a conductor in equilibrium must be entirely normal to the surface. Simultaneously, it is known that the electric field from any given object tends toward that of a point charge at a sufficiently large distance. Thus, the electric field very close to the target spacecraft is everywhere normal to the spacecraft surfaces, whereas the field at very far distances can be approximated by that of a point charge. At medium distances, the electric field is not easily determined. Analytical expressions exist for fields around some objects, such as rings, disks, or planes; however, for spacecraft representative shapes, these expressions become too complex to be widely applicable. Complex shapes, such as spacecraft, require the use of numerical routines to determine the electric field at medium distances. The development and implementation of a numerical program in MATLAB for modeling the electric fields and then simulating electron trajectories are presented in the Appendix. A hybrid approach is used to model the electric field: a high-fidelity method of moments (MOM) computation is performed to find the field close to a surface and a point-charge approximation is used for a point sufficiently far away from a surface. Although additional computational effort is required upfront to find the distance where the point-charge approximation is sufficiently accurate, the method is successful in achieving a desired accuracy with speed appropriate for

simulating large numbers of electrons. Throughout, it is assumed that the plasma Debye length is much longer than the separation distance between the target and the sensing spacecraft. Therefore, electric field and particle interactions with the ambient plasma are neglected. This assumption is generally valid in hot, sparse plasma environments, such as GEO or cislunar, where Debye lengths are on the order of tens to hundreds of meters [8,16].

B. Experimental Setup

To validate the numerical simulations, experiments were conducted in the Electrostatic Charging Laboratory for Interactions between Plasma and Spacecraft at the University of Colorado Boulder. The facility consists of a bell-jar-style vacuum chamber that is 22 in. in diameter with a nominal pressure during data collection between 10^{-5} and 10^{-6} torr. The target object for a given experiment was placed in the center of the chamber and irradiated with either a Kimball Physics EMG-4212 monoenergetic electron gun or a Hamamatsu L10706 vacuum ultraviolet (VUV) light source. Electron spectra produced by the target were measured with a custom-built retarding potential analyzer (RPA) and currents were read with a Keithley 2401 picoammeter. The RPA consists of a front grounded grid and a variable-voltage discriminating grid in front of a hollow cylinder collector. A range of high-voltage power supplies maintain the target object at a set potential or provide high voltage to the discriminating grid in the RPA. Additionally, a Stefan Mayer FLC3-70 magnetometer was used to measure the magnetic field. A 2-D motion system (one rotational stage and one linear stage) allows for simulated relative motion between the target and the sensor.

III. Spacecraft Shape Primitives

A. Experiment and Simulation Comparison

Experiments were conducted to measure currents of electron emitted from nontrivially shaped objects. The experimental results are directly compared to numerical results, which serves to validate the simulations. Once good agreement has been demonstrated between experiments and simulations, the simulations can then be used to investigate target objects that are not possible to test in the vacuum chamber.

A corner bracket was selected as a test shape because it contains several features that are relevant to spacecraft shapes. It has an exterior corner, which is similar to a box-shaped spacecraft bus. It contains an interior corner similar to a joint between a solar panel and a bus. Finally, edge effects, similar to looking at a solar panel edge on, are also captured. An aluminum 90 deg corner bracket 30.48 cm tall with sides 7.62 cm long was used as a target. As received, the bracket was very shiny and the aluminum had ink printed on it in several places. Photoemission is small for highly reflective surfaces and also depends strongly on the presence of contaminants on the surface. Therefore, the bracket was manually sanded with sandpaper and then cleaned with isopropyl alcohol before being installed in the chamber. The bracket was mounted on the rotary stage in the vacuum chamber, but electrically isolated from the stage. The bracket was held at −500 V and was exposed to VUV light to stimulate photoemission. Figure 2 shows the bracket in the vacuum chamber. The circle of
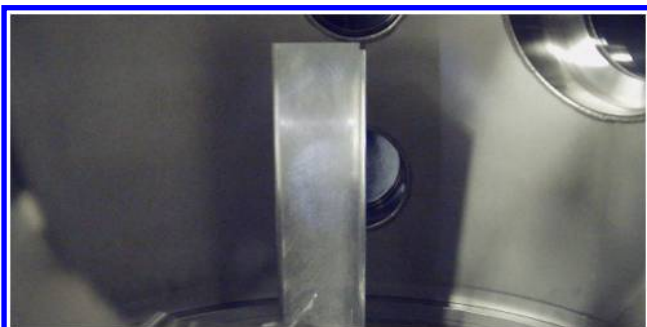
Fig. 2 Aluminum bracket in the vacuum chamber illuminated by the VUV light.

VUV light is visible in the center of the bracket. The RPA, located 30 cm from the target, was used to measure the electron current as the bracket was rotated. Vacuum chamber pressures during the experiment were on the order of 1 μtorr.

Figure 3 shows the MOM model of the bracket, which contains 864 triangular elements. The location of the RPA relative to the bracket is denoted by the black box. The charge on the bracket distributes such that the greatest charge is along the edges and at sharp corners. To simulate the emission of electrons from the bracket, particles are given initial conditions along the sides of the bracket in the $Z = 0$ plane. 800 total particles are simulated, with 200 along each of the four sides. Figure 4 shows the particle trajectories in the $Z = 0$ plane. The particles are generated with equal spacing along each edge, so the relative density of the particle trajectories (black lines) is representative of what current would be measured by a sensor in a given location. A simulated sensor with the same dimensions as the RPA is swept around the bracket, and the number of particles that enter the detector is counted at each angle step.

In the experiment, the current is directly measured in nano-amperes; however, the simulated signal is in number of particles. To facilitate comparison between simulated signal and experimentally measured current, the simulated signal needs to be multiplied by a scale factor because the photoemission efficiency of the surfaces is unknown. The scale factor is selected to minimize the least-squares error between the simulated signal and the experimentally measured current. Comparison between the simulated and experimentally measured signals is shown in Fig. 5. The zero
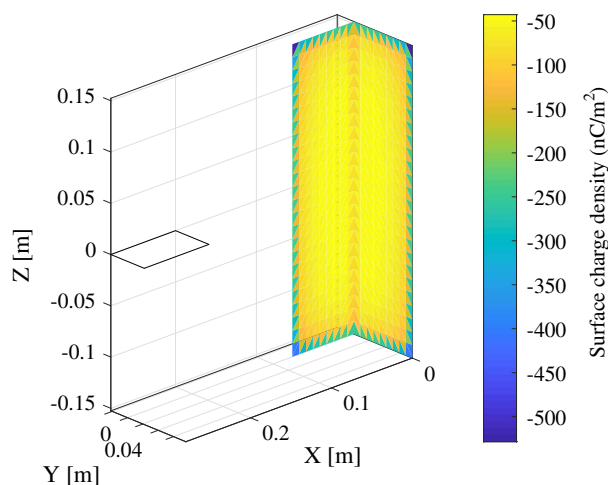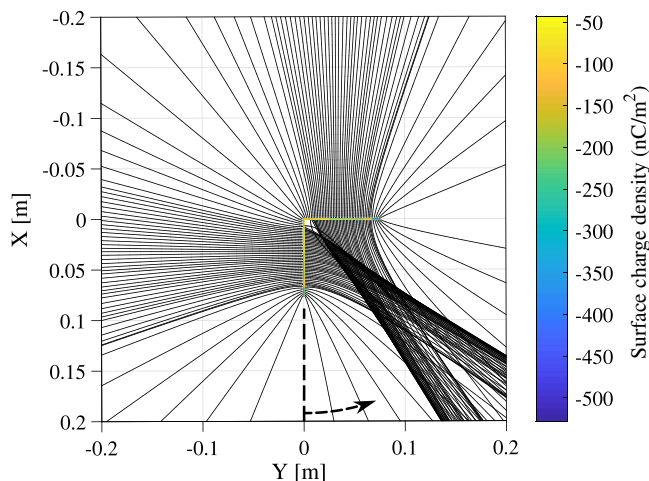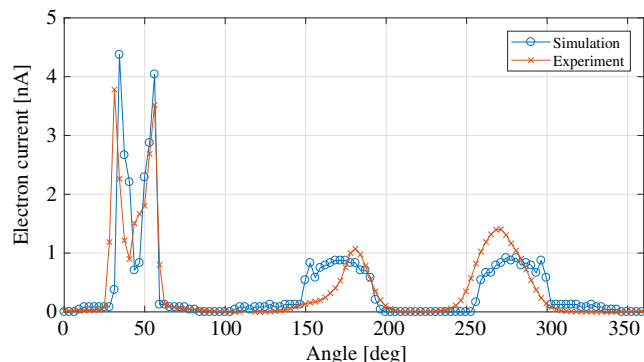

Fig. 5   Comparison of experimental and simulated signals emitted from rotating bracket.

angle is defined as the $+X$ axis (i.e., the bottom of Fig. 4), with positive angle defined in the right-hand sense (counterclockwise from the $+X$ axis).

Overall agreement is obtained between the simulation and experimental results. It is clear that no particles are emitted in the edge-on directions (at angles of 0 and 90 deg). The electric field very close to the bracket surface is everywhere normal to the bracket, so the electric field near the edges changes very quickly from one side of the bracket to the other. Thus, a very small region in initial location maps to large differences in final location, which causes the spreading and decrease in signal. The interior corner acts as a lens that focuses the particles generated on those faces into a beam directed at an angle of 45 deg. There is a double-peak structure present as the trajectories of particles from the interior faces cross and diverge. The double-peak structure is captured well by both the simulation and experimental results. At 180 and 270 deg, there is a signal increase due to particles emitted from the flat exterior sides of the bracket. There is a difference of approximately 26% in signal magnitude between the experimentally measured peaks at these locations. Ideally, both sides of the bracket are identical, and so the peaks should also be identical. The VUV light has an output stability better than 1%, and so any significant changes in the source can be ruled out. One likely explanation for the discrepancy is differences in the surface condition of each side. The bracket was sanded manually, and it is known that variations in surface roughness or the presence of contaminants causes variations in the photoelectron yield [17]. Repetition of the experiment using more precise surface preparation and characterization methods may result in improved agreement between the simulation and the experiment in the regions around 180 and 270 deg. The objective of this experiment, however, was to demonstrate that the numerical models capture the physics of electron emission from charged spacecraft-representative shapes. Overall agreement between simulations and experiments demonstrates that this objective is achieved.

B.   Spacecraft Models

The numerical simulations are now used to consider electron emission from a variety of representative spacecraft models. Only the planar case is considered here, so all electrons are generated in the $Z = 0$ plane. This assumption allows for analytical understanding of the effect of spacecraft geometry to be obtained, which can then be extended to three dimensions. Similarly, initial energy and angle distributions of secondaries and photoelectrons are neglected as this allows the effects of the spacecraft geometry to be investigated more clearly. Each spacecraft model is charged to -500 V. First, a spacecraft consisting of a box with two identical solar panels is modeled. The entire spacecraft is assumed to be electrically conducting, in accordance with satellite design recommendations [18,19]. Figure 6 shows an MOM model of the box-and-panel spacecraft along with electron trajectories emitted from every surface. Again, particles are generated with equal spacing, so the density of trajectories in a given area is representative of signal strength.

Several key trends are visible in Fig. 6b. Flat surfaces, such as the sides of the box or the solar panels, produce electron signals that are

Fig. 3   MOM model of bracket.

Fig. 4   Simulation of electrons emitted from bracket.

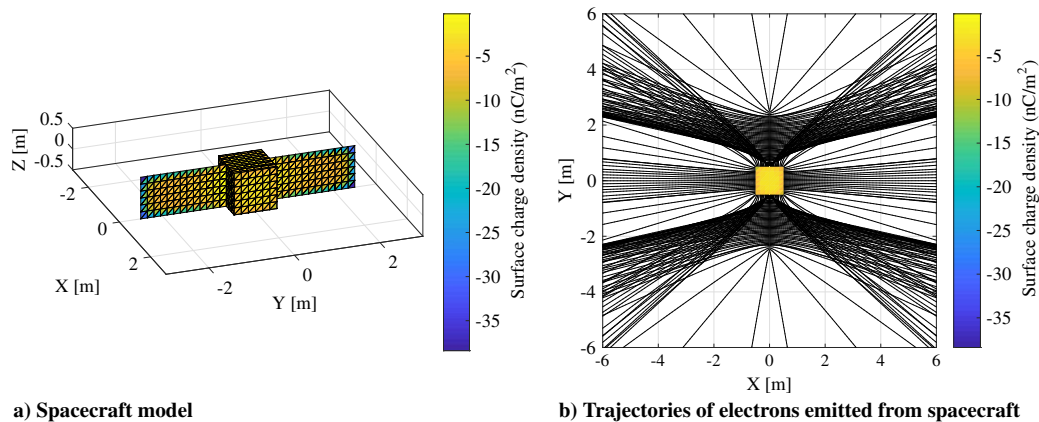a) Spacecraft model   b) Trajectories of electrons emitted from spacecraft

Fig. 6   Box spacecraft with two solar panels.

sufficiently large to measure. Interior corners serve to focus the electron signal, whereas zero signal is observed when viewing a panel edge on. In this case, the spreading effect, which is expected at the corners of the box, is dominated by the focusing effect from the box–panel joint.

Figure 7 shows the trajectories for particles emitted by a cylindrical spacecraft with two solar panels. The resulting pattern is very similar to the box, except that there is a spreading effect around the $Y = 0$ axis. The curved surface of the cylinder causes the particles to diverge more in this region compared to the flat surface of the box.

Next, a parabolic dish is modeled, as shown in Fig. 8. The geometry of the dish focuses the particles generated on the concave side into a beam, whereas those on the convex side are spread out over a wide area. Depending on the absolute signal magnitude as well as the

capabilities of a given sensing craft, either of these cases may be advantageous. If a sensor is capable of measuring the signal emitted from the convex side of the dish, the signal is available for a much larger region. Thus, the potential of the dish could be measured for a longer period of time if the dish was tumbling in space. On the other hand, the signal emitted from the concave side is larger, which would produce a larger signal-to-noise ratio and perhaps a higher confidence measurement of the potential. However, this signal would only be available during limited windows of time in a situation with relative motion between the sensor and the target. Additionally, the secondary and photocurrents produced on concave surfaces may be lower because the incident currents and solar illumination are reduced due to self-shadowing from the space environment. Convex surfaces, on the other hand, are not shadowed from the environment, so
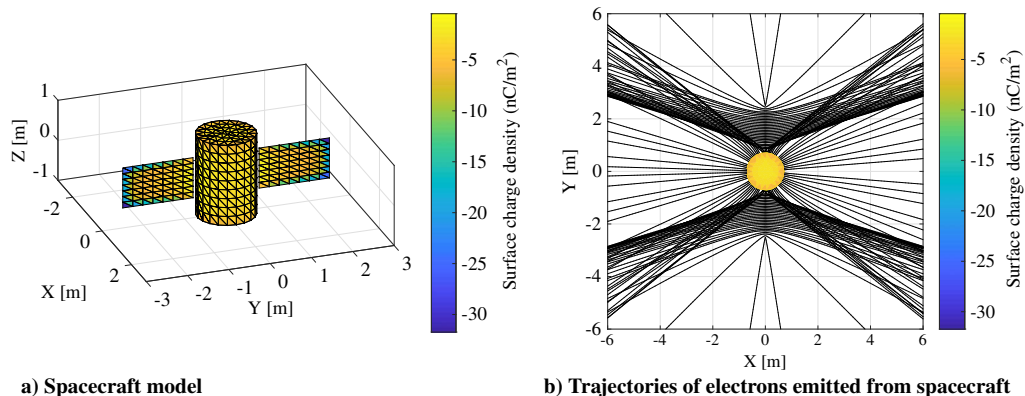

a) Spacecraft model   b) Trajectories of electrons emitted from spacecraft

Fig. 7   Cylindrical spacecraft with two solar panels.

a) Parabolic dish model   b) Trajectories of electrons emitted from parabolic dish

Fig. 8   Parabolic dish antenna.

a) Spacecraft model   **b) Trajectories of electrons emitted from spacecraft**
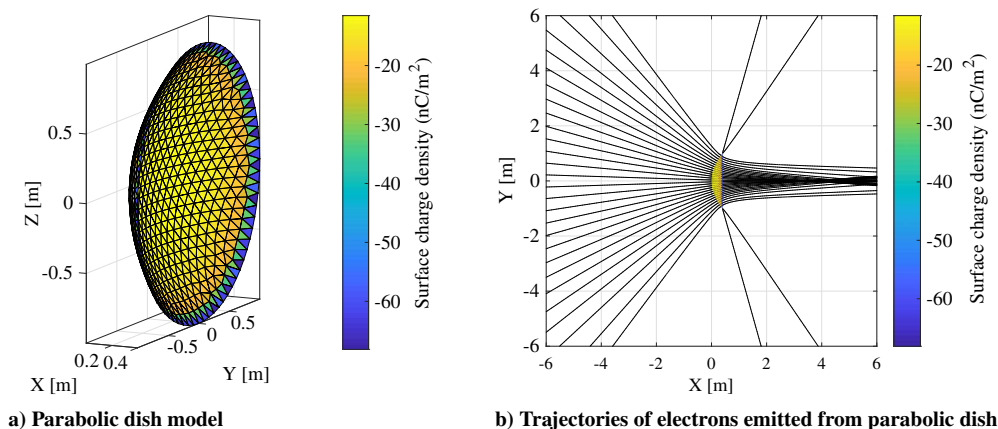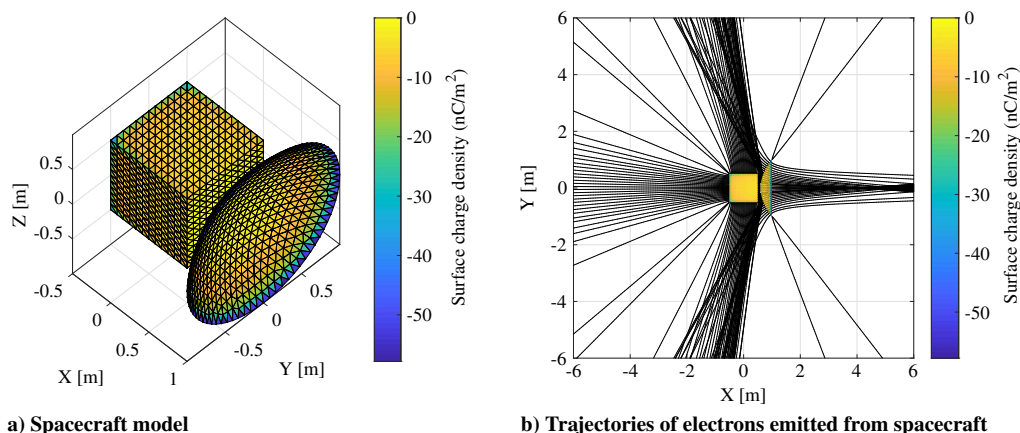
Fig. 9   Box spacecraft with a parabolic dish antenna.

incident currents and illumination may be higher when compared to concave surfaces.

Finally, a box spacecraft with an antenna dish is modeled, as shown in Fig. 9. The highest signal regions come from the interior corners where the box and dish are joined, as well as the concave surface of the dish. The lowest signal magnitudes are emitted from the corners of the box and from the edges of the dish.

The insights obtained are summarized as follows:

1) There always exists some point on the target spacecraft for which electrons map back to the servicing spacecraft. However, this area may be very small and the resultant signal may be very difficult to measure. A tradeoff exists between the capability of a detector and the regions over which measurement of target potential is possible.

2) Regions of low signal include convex surfaces, such as exterior corners and edges. The sharper the corner or edge is, the greater is the spreading effect of the electron signal emitted from that location. For example, no signal is obtained by looking at a panel edge on. The relative signal from a curved surface (such as a cylinder) is greater than that from a hard corner (such as that of a box).

3) Concave surfaces, such as interior corners, focus particles from different surfaces into the same direction in space. This produces relatively large signals, but over limited spatial regions.

IV.   Differential Charging

Spacecraft design best practices recommend all exterior surfaces be connected to a common ground to prevent differential charging, which can result in hazardous arcing [18,19]. Despite this recommendation, numerous spacecraft are known to become differentially charged and experience arcing (e.g., [20]). This presents an interesting case for touchless sensing because there is not just one target potential to be measured, and the electric fields from differentially charged spacecraft components may guide the electrons in unexpected directions. To

investigate touchless sensing of differentially charged spacecraft, two side-by-side plates at different potentials are considered.

Figure 10 shows results from a simulation for particles emitted from two differentially charged plates. The plate on the left is charged to −1000 V and the plate on the right is charged to −500 V. Particles emitted from the left plate (thus having energies of 1000 eV) are plotted in blue and those from the right plate (with energies of 500 eV) are plotted in red. Several interesting features are visible in the simulation results. First, the charge density on the inner side of the right-hand plate is positive, even though the plate is held at a negative potential. The close proximity to the −1000 V plate forces the negative charges to the outside edge, creating a positive charge distribution on the inside edge. The charge distribution of the −1000 V plate is not significantly affected by the presence of the −500 V plate on the right. Similarly, the higher energy population of electrons emitted from the left plate (blue lines) is not affected by the electric field from the right plate. Conversely, the electrons emitted from the right plate (red lines) are steered significantly in the +Y direction. In fact, particles generated very close to the inner edge of the −500 V plate are unable to overcome the potential barrier imposed by the −1000 V plate and do not escape at all. For a sensor located at a −Y coordinate, only the potential of the left plate would be sensed because no electrons from the right plate travel in the −Y direction. For a sensor located at a +Y coordinate, both the 1000 and 500 eV populations are observed, so the potentials of both plates are sensed. A sensor sweeping around these two targets would be able to determine which potential is on which plate.

To confirm this hypothesis, an experiment was conducted in which two aluminum plates were placed side by side in the vacuum chamber and charged to different potentials. The plates were then illuminated with the VUV light to stimulate photoemission. The plates were kept in place with the RPA mounted on a rotating arm and swept around the target. Figure 11 shows a picture of the experimental setup. The RPA angle α is defined relative to the +X axis, as given in Fig. 11b.
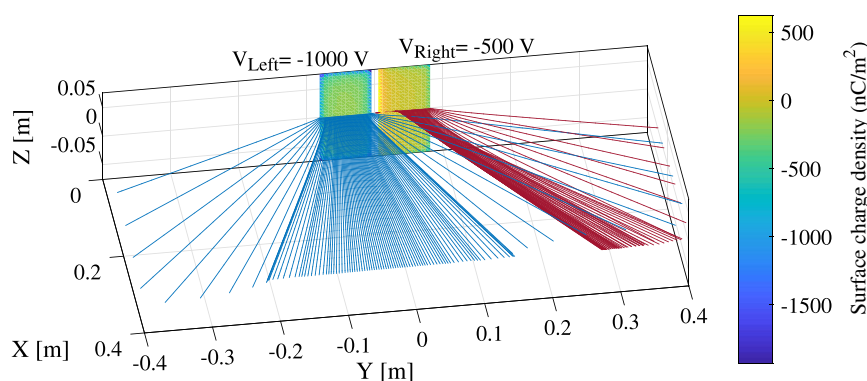

Fig. 10   Simulation of electrons emitted from differentially charged plates.
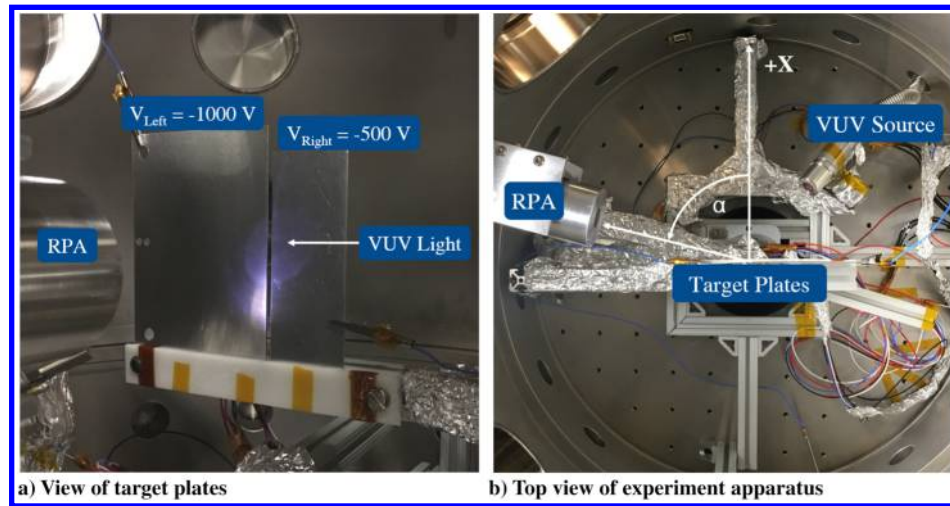
Fig. 11   Experiment apparatus to test sensing of differentially charged targets.
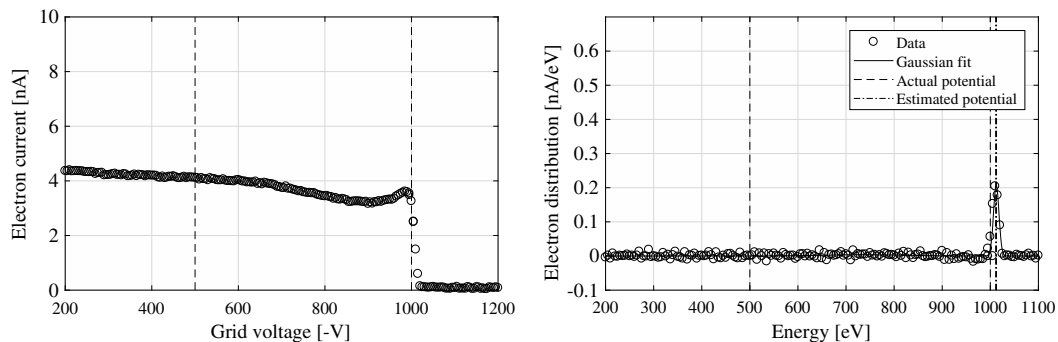

Fig. 12   Spectrum of electrons emitted from differentially charged plates taken with the RPA located at an angle of 30 deg.

Figure 12 shows a spectrum taken by the RPA when it was located at an angle of 30 deg. At this angle, only the 1000 eV population is observed. This is consistent with the simulation results shown in Fig. 10, which shows the particles from the −500 V plate being steered in the $+Y$ direction. Figure 13 shows a spectrum taken with the RPA at an angle of 50 deg. At this location, both the 500 and 1000 eV populations are observed, indicating that a single spectrum can be used to determine multiple potentials on a target object. At this angle, the 500 eV peak is significantly larger than the 1000 eV, which is also consistent with the simulations.

The agreement between the experimental and numerical results demonstrates that touchless sensing is feasible for differentially charged target objects. However, the complex electric fields near such targets affect the spatial locations at which one or both potentials can be measured. Several factors should be considered when extending these results to the spacecraft scale. It is apparent that the

magnitude of voltage difference between two components plays an important role. For example, the sensing effects of two components charged 50 V different are much less than those of two components charged 5 kV different. The relative sizes of the differentially charged components being sensed are also important. For example, if an entire solar panel is floating at a different potential from a spacecraft bus, the sensing process is substantially affected. Conversely, if a single cell on the solar panel is floating at a different potential from the rest of the panel, the effects on the sensing process may be small.

To illustrate this effect, a simulation is conducted for a differentially charged box-and-panel spacecraft model, in which the box is charged to −1000 V and the panel is charged to −600 V. In general, the distribution of potentials across a spacecraft surface may be more complicated than the simplified model considered here, depending on spacecraft design, materials, and grounding. The box-and-panel model, however, is useful for demonstrating the effect of differentially
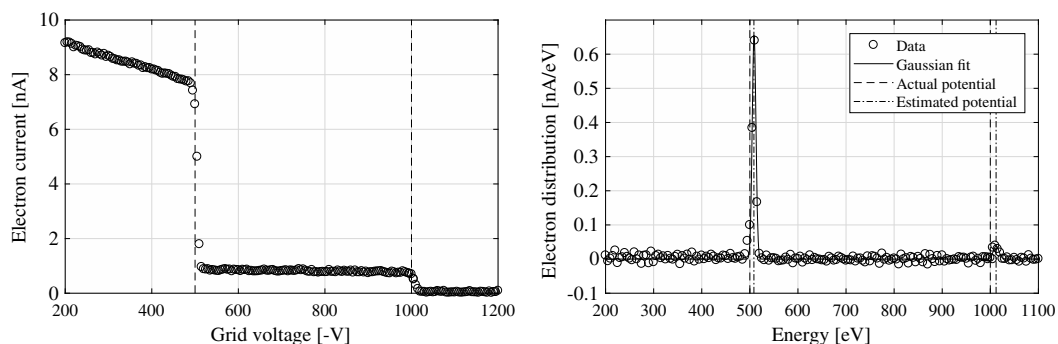

Fig. 13   Spectrum of electrons emitted from differentially charged plates taken with the RPA located at an angle of 50 deg.
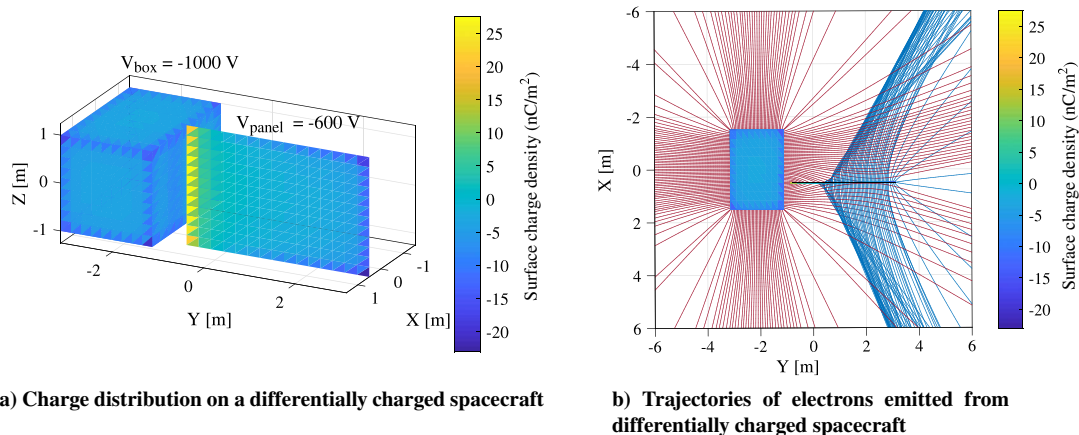
a) Charge distribution on a differentially charged spacecraft

b) Trajectories of electrons emitted from differentially charged spacecraft

Fig. 14   Differentially charged spacecraft, in which the box is charged to −1000 V and the panel is charged to −600 V.

a) Charge distribution on a homogeneously charged spacecraft

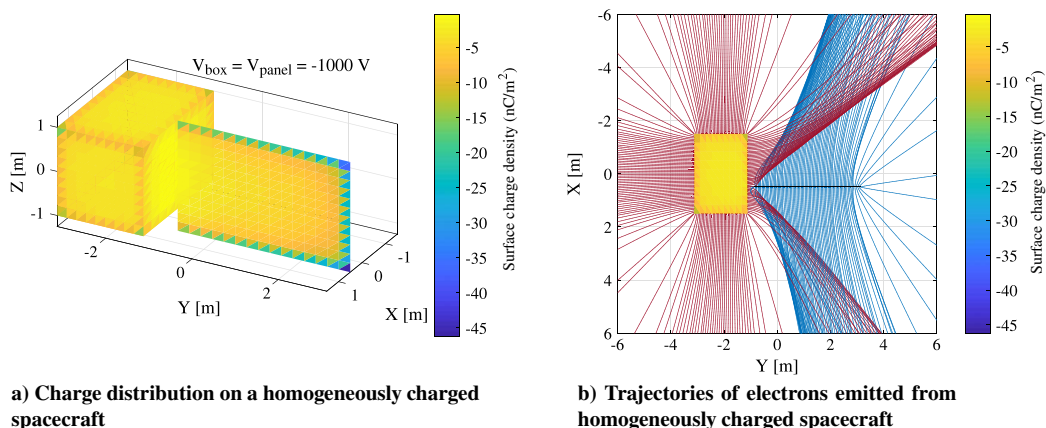**b) Trajectories of electrons emitted from homogeneously charged spacecraft**

Fig. 15   Homogeneously charged spacecraft, in which the box and panel are both charged to −1000 V.

charged surfaces on the sensing process. The MOM model for the differentially charged craft is shown in Fig. 14a, and the trajectories of electrons emitted from the craft are shown in Fig. 14b. For comparison, the electrostatic model and trajectories for a spacecraft of the same shape but homogeneously charged to −1000 V are shown in Fig. 15. To aid in understanding the trajectories, particles originating on the box are plotted in red, whereas those originating on the panel are plotted in blue. In the homogeneous case, the electrons emitted from the right side of the box are significantly deflected away from the panel. Similarly, those emitted from the panel are also deflected away from the box. In the differential charging case, however, the electrons emitted from the right side of the more negatively charged box are only slightly perturbed by the presence of the panel. As a result, the population of electrons emitted from the box is visible in a larger spatial region, specifically near the panel edge, than in the homogeneous charging case. Those emitted from the panel, however, are strongly steered away in the $+Y$ direction due to the electric field of the box. The electrostatic models show that when the panel is differentially charged relative to the box, a positive charge resides on the leftward side of the panel. As a result, electrons originating on the left side of the panel are unable to escape from the surface. Once again, the relative location of the sensing craft determines which electron population is measurable. In the differential charging case, the 600 eV population from the panel is present only in narrower spatial region than the homogeneous case. Both electron populations would be measurable in some specific areas.

When an electron beam is used for active sensing, only those surfaces that are hit with the beam generate electrons. It would be possible to sense the potential of one surface at a time by deflecting and focusing the electron beam to hit a specific surface. For the passive sensing case, in which sunlight is used to stimulate photo-emission, numerous spacecraft surfaces emit photoelectrons simultaneously, so multiple populations may be present in the electron spectra.

V.   Conclusions

A hybrid MOM/point-charge method has been developed for accurate modeling of electric fields. This approach combines the accuracy of MOM very close to a charged surface with the speed of point-charge evaluations at larger distances. The numerical program has been used to model the trajectories of charged particles emitted from various spacecraft-representative shapes. Experiments have been conducted, in which a bracket at a large voltage was illuminated with VUV light. The current emitted from the bracket was measured as a function of rotation angle, and agreement is achieved between the experiment and the simulation. Electron emission from model spacecraft has been simulated for various combinations of boxes, panels, cylinders, and dishes. It is found that concave surfaces and inside corners focus electrons into a localized spatial region, thus creating a large relative current, although the absolute signal magnitude may be reduced for concave surfaces due to self-shadowing from sunlight or environmental currents. Exterior corners and convex surfaces spread electrons out over a large spatial region. This results in a smaller relative signal, but over a larger area. Either of these cases may be desirable depending on the overall signal magnitude and capabilities of the detector. Finally, experiments and simulations have been conducted to study sensing of simplified differentially charged targets. Simultaneous touchless sensing of two surfaces at different potentials has been demonstrated.

Appendix A: Electric Field Modeling

A hybrid approach is used to model the electric field: the MOM computation is performed to find the field close to a surface and a point-charge approximation is used for points sufficiently far away from a surface. The development of both techniques is described as follows, along with determination of the distance away from a surface at which the point-charge approximation can be used.

First, the geometry of the model object is either imported as a stereolithography file or defined in the MATLAB program. Delaunay triangulation is used to discretize the object into triangular elements [21]. Next, MOM is used to compute the elastance matrix for the system S [22]. Method of moments is based on the following equation for voltage:

$$V(\mathbf{r}) = \int \frac{\mathrm{d}q'}{4\pi\epsilon_0 |\mathbf{r} - \mathbf{r}'|} \tag{A1}$$

where $\mathrm{d}q'$ is a differential charge element located at point $\mathbf{r}'$, and V is the voltage due to that element observed at point $\mathbf{r}$. For a charged object discretized into N finite areas, the voltage is found by summing the integral over each area A_i that has a surface charge density σ_i:

$$V(\mathbf{r}) = \frac{1}{4\pi\epsilon_0} \sum_{i=1}^{N} \int_{A_i} \frac{\mathrm{d}A'}{|\mathbf{r} - \mathbf{r}'_i|} \sigma_i \tag{A2}$$

The voltage at the center of each discrete element is found by arranging Eq. (A2) into matrix form:

$$\begin{bmatrix} V_1 \\ V_2 \\ \vdots \\ V_N \end{bmatrix} = \frac{1}{4\pi\epsilon_0} \begin{bmatrix} \int_{A_1} \frac{\mathrm{d}A'}{A_1|r_1-r'|} & \cdots & \int_{A_N} \frac{\mathrm{d}A'}{A_N|r_1-r'|} \\ \int_{A_1} \frac{\mathrm{d}A'}{A_1|r_2-r'|} & \cdots & \int_{A_N} \frac{\mathrm{d}A'}{A_N|r_2-r'|} \\ \vdots & \ddots & \vdots \\ \int_{A_1} \frac{\mathrm{d}A'}{A_1|r_N-r'|} & \cdots & \int_{A_N} \frac{\mathrm{d}A'}{A_N|r_N-r'|} \end{bmatrix} \begin{bmatrix} Q_1 \\ Q_2 \\ \vdots \\ Q_N \end{bmatrix} \tag{A3}$$

The $N \times N$ matrix is the elastance matrix S (which has a unit of F^{-1}). Given the Delaunay triangulation of the model, the elastance matrix is computed in the triangular basis using a routine developed by Hughes and Schaub [23]. Once the elastance matrix has been computed, voltages are assigned for each triangle element. In most cases, the entire object is assumed to be conducting, and so all elements have the same voltage. For the case of differential charging, the triangle elements representing one spacecraft component (e.g., a panel) all have the same voltage, and all the elements representing a different component (e.g., the spacecraft bus) have a different voltage. Given the elastance matrix and the voltages, the charge on each triangle element can then be computed:

$$Q = S^{-1}V \tag{A4}$$

where Q is an $N \times 1$ vector, which contains the total charge on each triangle element in coulombs, and V is the $N \times 1$ vector describing the voltage on each element in volts.

Now, given the location and charge of each triangle, the electric field can be determined by summing the contribution of the integral over each triangle:

$$E(\mathbf{r}) = \frac{1}{4\pi\epsilon_0} \sum_{i=1}^{N} \int_{A_i} \frac{\sigma_i(\mathbf{r} - \mathbf{r}'_i)}{|\mathbf{r} - \mathbf{r}'_i|^3} \, \mathrm{d}A' \tag{A5}$$

This step is also computed numerically using an algorithm from Ref. [23]. Note that this approach requires integrating over each triangular element, and then summing all of the integrals to find the electric field at a given point.

The MOM formulation provides excellent accuracy, but is relatively slow because it requires a computationally expensive integral for each triangular element. However, at a sufficiently large distance away, the difference between the electric field from the triangle and the electric field from a representative point charge in the same place is negligible. The electric field of a point charge has a simple analytical form, so the expensive numerical integrals can be avoided. Therefore, a hybrid method is developed, in which the full MOM integral is used for the contribution from elements near the test point, whereas the point-charge approximation is used to determine the contribution from faraway elements. The next section addresses the question: how far is sufficiently far for the point-charge approximation to be applied? Note that the point-charge approximation is based on the multisphere method (MSM), in which a spacecraft is modeled as a collection of finite radius spheres [24,25]. The primary difference between MSM and the point-charge approximation is that MSM uses spheres with nonzero radius, and so it can accurately model the capacitance of a spacecraft. In the present case, there is no need to consider capacitance; thus, the point-charge model is sufficient. The point-charge approach is faster than heterogeneous MSM approaches [23] because it does not require additional calculations to determine the appropriate size of each sphere.

Figure A1 shows a model spacecraft represented as MOM triangular elements, a collection of point charges, and as a hybrid of triangles and points. For the hybrid example, the point $(X, Y, Z) = (0.5, 0, 0.5)$ m is taken as an example measurement point. Elements in the immediate vicinity of the measurement point are modeled as triangles, whereas elements beyond a threshold distance are modeled as point charges.

The distance from a given triangle where the point-charge approximation is sufficiently accurate depends on the charge and size of the triangle. To determine this distance, a single triangular element is considered. The triangle voltage is varied from -100 V to -15 kV, and the size of the triangle is varied from 0.005 to 0.5 m. The electric field at 10,000 points near the triangle is computed at every voltage and size using both the full MOM and the point charge approximation. Then, the distance is found such that each component of the MOM electric field and point-charge field matches to $<0.1 \ \mathrm{V} \cdot \mathrm{m}^{-1}$. Percentage difference is not well defined because both fields are converging to zero as a function of increasing distance, and so absolute difference is used instead. A threshold error of $0.1 \ \mathrm{V} \cdot \mathrm{m}^{-1}$ is selected because, in most cases of interest, the target object is charged to several hundred volts. Assume, for example, that there is a potential difference of 500 V between two craft with a separation distance of 10 m. This gives an electric field between the objects of $50 \ \mathrm{V} \cdot \mathrm{m}^{-1}$. Thus, a difference in electric field of $0.1 \ \mathrm{V} \cdot \mathrm{m}^{-1}$ represents an error of 0.2%. For larger voltages or smaller separation distances, the error decreases.

Figure A2 shows an example of the differences between the MOM and point charge at 10,000 points around a 1 cm triangular element at -1000 V. The electric field of the triangle and the representative point charge match to within $0.1 \ \mathrm{V} \cdot \mathrm{m}^{-1}$ at a distance of 0.1363 m away (denoted by the black lines). This same process is repeated for the other triangle sizes and charge densities to determine the error threshold distance as a function of both the triangle element size and charge.

A 2-D polynomial with the following form is fit to these data points:

$$d = p_{00} + p_{01}L + p_{10}Q + p_{20}L^2 + p_{11}LQ + p_{02}Q^2 \tag{A6}$$

where d is the error threshold distance, Q is the charge on the triangle, L is the length of one side of the triangle, and p_{xx} are fitting parameters. Figure A3 shows the data points and the fit function, which has an R^2 value of 0.9941. In all simulations presented in this work, MOM is used to find the contribution to the total electric field from triangles less than a distance d away, and all triangles more than a distance d away are approximated as point charges. This hybrid MOM/point-charge method provides a computationally efficient simulation framework with both near-surface and far-field accuracy, plus sufficient speed to simulate large numbers of electrons.

a) Method of Moments model

b) Point charge model

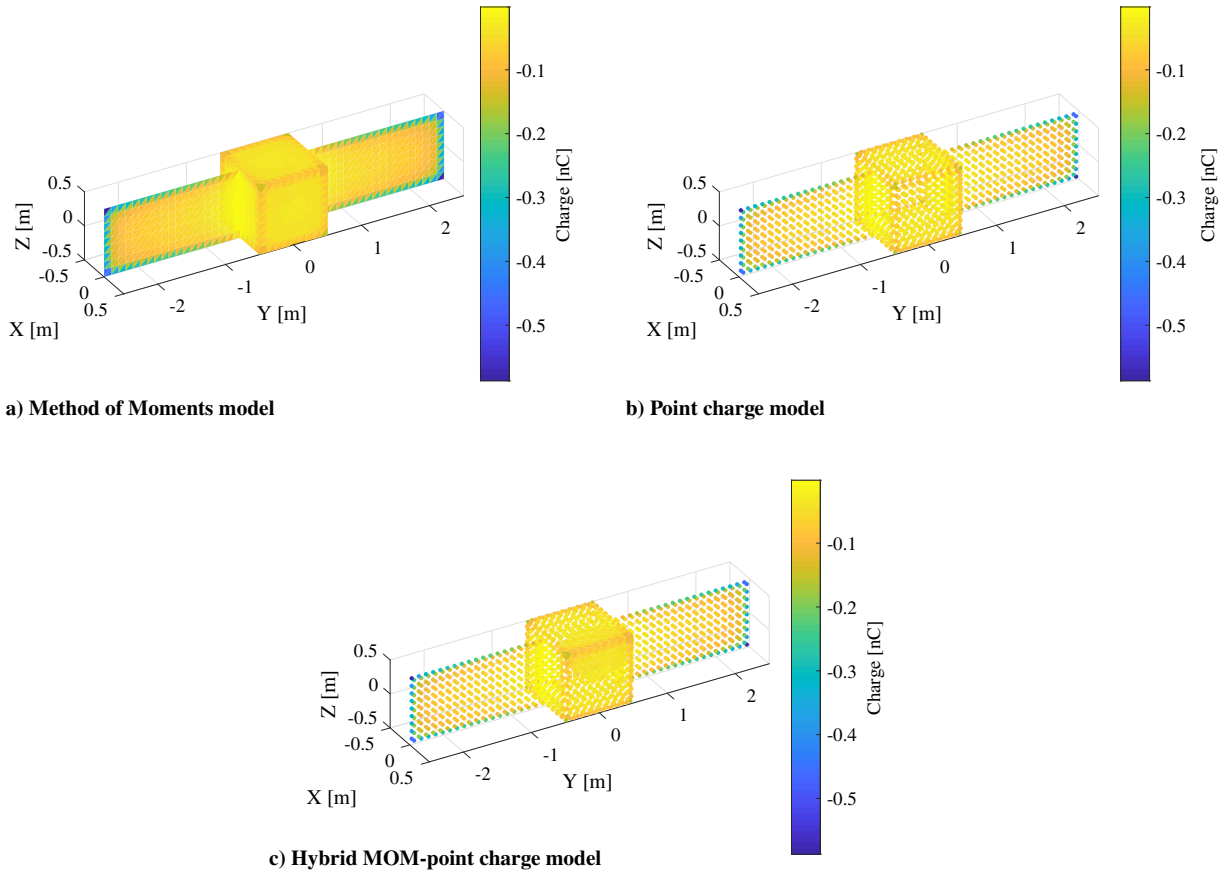c) Hybrid MOM-point charge model

Fig. A1   Various electrostatic models of a spacecraft.
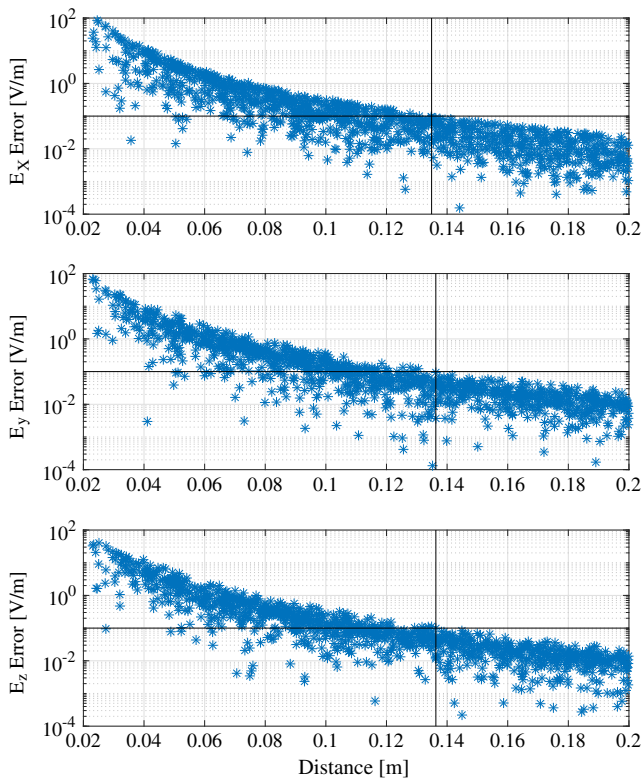

Fig. A2   Difference between MOM and point-charge electric fields for 10,000 points around a triangular element.
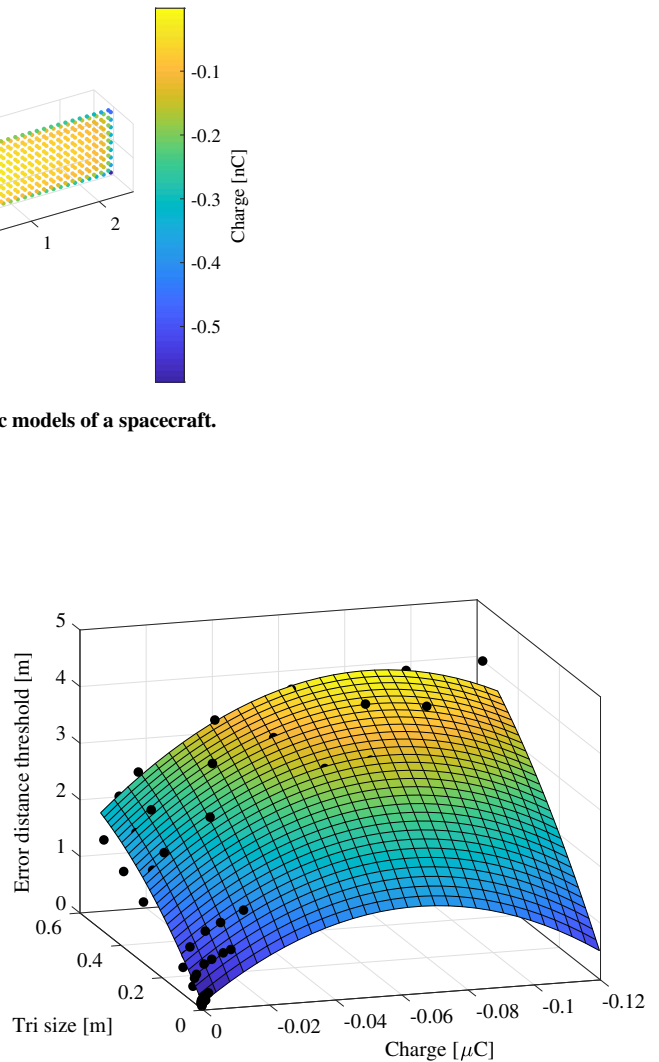

Fig. A3   Threshold distance at which the point-charge approximation of a triangular element matches the MOM electric field from that element to within $0.1 \ \mathrm{V} \cdot \mathrm{m}^{-1}$.

Appendix B: Charged Particle Dynamics

Once the charge distributions and electric field are computed, the trajectories of electrons emitted from the charged spacecraft can be studied. The force on each electron at each time step is given by Lorentz force:

$$\boldsymbol{F} = q(\boldsymbol{E} + \boldsymbol{v} \times \boldsymbol{B}) \tag{B1}$$

Table A1 Fitting parameters for Eq. (A6)

Parameter	
p_{00}	0.08025
p_{01}	6.049
p_{10}	−43.58
p_{20}	−4.2
p_{11}	−20.66
p_{02}	−336.8

where q is the electron charge, v is the velocity of each particle, and B is the magnetic field. The magnetic field is assumed to be zero, although the simulation framework is developed such that a nonzero field can be modeled if desired. Mutual repulsion between electrons is neglected. Similarly, no interactions with plasma in the surrounding environment are assumed. Secondary and photoelectrons are emitted with small initial energies and angular distributions (e.g., [17,26]). However, the objective of this work was to gain insight into how the geometry of a spacecraft guides and focuses emitted electron fluxes. Therefore, the emitted particles are assumed to have zero initial energy.

Given the electric field, Lorentz force, and initial conditions, the electron motions are integrated using the Boris algorithm, which is the standard for simulating the motion of charged particles in electric and magnetic fields [27,28]. Runge–Kutta integrators, which are commonly used in other dynamics simulations, do not conserve constants of motion, such as gyromotion or energy, in charged particle simulations. Boris algorithm is a leapfrog-type method, which conserves constants of motion for charged particles. This algorithm is implemented as follows:

$$h = \frac{qB\mathrm{d}t}{2m} \tag{B2}$$

$$s = \frac{2h}{1 + h \cdot h} \tag{B3}$$

$$v^- = v_j + \left(\frac{q}{2m}\right)E\mathrm{d}t \tag{B4}$$

$$v' = v^- + v^- \times h \tag{B5}$$

$$v^+ = v^- + v' \times s \tag{B6}$$

$$v_{j+1} = v^+ + \left(\frac{q}{2m}\right)E\mathrm{d}t \tag{B7}$$

$$x_{j+1} = x_j + v_{j+1}\mathrm{d}t \tag{B8}$$

where x_j and v_j are the position and velocity vectors at a time step j, respectively, and h, s, v', v^+, and v^- are intermediate calculations.

Acknowledgments

References

[1] Ferguson, D. C., Murray-Krezan, J., Barton, D. A., Dennison, J. R., and Gregory, S. A., "Feasibility of Detecting Spacecraft Charging and Arcing by Remote Sensing," *Journal of Spacecraft and Rockets*, Vol. 51, No. 6, 2014, pp. 1907–1913. https://doi.org/10.2514/1.A32958

[2] Anderson, P. V., and Schaub, H., "Local Debris Congestion in the Geosynchronous Environment with Population Augmentation," *Acta Astronautica*, Vol. 94, No. 2, 2014, pp. 619–628. https://doi.org/10.1016/j.actaastro.2013.08.023

[3] Oltrogge, D. L., Alfano, S., Law, C., Cacioni, A., and Kelso, T. S., "A Comprehensive Assessment of Collision Likelihood in Geosynchronous Earth Orbit," *Acta Astronautica*, Vol. 147, June 2018, pp. 316–345. https://doi.org/10.1016/j.actaastro.2018.03.017

[4] Ellery, A., Kreisel, J., and Sommer, B., "The Case for Robotic On-Orbit Servicing of Spacecraft: Spacecraft Reliability Is a Myth," *Acta Astronautica*, Vol. 63, Nos. 5–6, 2008, pp. 632–648. https://doi.org/10.1016/j.actaastro.2008.01.042

[5] Flores-Abad, A., Ma, O., Pham, K., and Ulrich, S., "A Review of Space Robotics Technologies for On-Orbit Servicing," *Progress in Aerospace Sciences*, Vol. 68, July 2014, pp. 1–26. https://doi.org/10.1016/j.paerosci.2014.03.002

[6] Xu, W., Liang, B., Li, B., and Xu, Y., "A Universal On-Orbit Servicing System Used in the Geostationary Orbit," *Advances in Space Research*, Vol. 48, No. 1, 2011, pp. 95–119. https://doi.org/10.1016/j.asr.2011.02.012

[7] McKnight, D., "Pay Me Now or Pay Me More Later: Start the Development of Active Orbital Debris Removal Now," *Advanced Maui Optical and Space Surveillance Technologies Conference*, 2010.

[8] Schaub, H., and Moorer, D. F., "Geosynchronous Large Debris Reorbiter: Challenges and Prospects," *Journal of the Astronautical Sciences*, Vol. 59, Nos. 1–2, 2012, pp. 161–176. https://doi.org/10.1007/s40295-013-0011-8

[9] Bengtson, M., Wilson, K., Hughes, J., and Schaub, H., "Survey of the Electrostatic Tractor Research for Reorbiting Passive GEO Space Objects," *Astrodynamics*, Vol. 2, No. 4, 2018, pp. 291–305. https://doi.org/10.1007/s42064-018-0030-0

[10] Aslanov, V., and Schaub, H., "Detumbling Attitude Control Analysis Considering an Electrostatic Pusher Configuration," *Journal of Guidance, Control, and Dynamics*, Vol. 42, No. 4, 2019, pp. 900–909. https://doi.org/10.2514/1.G003966

[11] Bennett, T., Stevenson, D., Hogan, E., and Schaub, H., "Prospects and Challenges of Touchless Electrostatic Detumbling of Small Bodies," *Advances in Space Research*, Vol. 56, No. 3, 2015, pp. 557–568. https://doi.org/10.1016/j.asr.2015.03.037

[12] Schaub, H., Parker, G. G., and King, L. B., "Challenges and Prospects of Coulomb Spacecraft Formation Control," *Journal of Astronautical Sciences*, Vol. 52, No. 1, 2004, pp. 169–193. https://doi.org/10.1007/BF03546427

[13] Goodman, M., Paez, A., Willis, E., and DeStefano, A., "An Analytic Model for Estimating the First Contact Resistance Needed to Avoid Damaging ESD During Spacecraft Docking in GEO," *Applied Space Environments Conference*, 2019.

[14] Bengtson, M., Wilson, K., and Schaub, H., "Experimental Results of Electron Method for Remote Spacecraft Charge Sensing," *Space Weather*, Vol. 18, No. 3, 2020, Paper e2019SW002341. https://doi.org/10.1029/2019SW002341

[15] Bengtson, M., Hughes, J., and Schaub, H., "Prospects and Challenges for Touchless Sensing of Spacecraft Electrostatic Potential Using Electrons," *IEEE Transactions on Plasma Science*, Vol. 47, No. 8, 2019, pp. 3673–3681. https://doi.org/10.1109/TPS.2019.2912057

[16] Schaub, H., and Sternovsky, Z., "Active Space Debris Charging for Contactless Electrostatic Disposal Maneuvers," *Advances in Space Research*, Vol. 53, No. 1, 2014, pp. 110–118. https://doi.org/10.1016/j.asr.2013.10.003

[17] Feuerbacher, B., and Fitton, B., "Experimental Investigation of Photoemission from Satellite Surface Materials," *Journal of Applied Physics*, Vol. 43, No. 4, 1972, pp. 1563–1572. https://doi.org/10.1063/1.1661362

[18] Purvis, C. K., Garrett, H. B., Whittlesey, A., and Stevens, N. J., "Design Guidelines for Assessing and Controlling Spacecraft Charging Effects," NASA TP 2361, 1984.

[19] Garrett, H. B., and Whittlesey, A. C., *Guide to Mitigating Spacecraft Charging Effects*, Vol. 3, Wiley, Hoboken, NJ, 2012, Chap. 3.

[20] Ferguson, D., White, S., Rast, R., and Holeman, E., "The Case for Global Positioning System Arcing and High Satellite Arc Rates," *IEEE Transactions on Plasma Science*, Vol. 47, No. 8, 2019, pp. 3834–3841. https://doi.org/10.1109/TPS.2019.2922556

[21] Persson, P.-O., and Strang, G., "A Simple Mesh Generator in MAT-LAB," *SIAM Review*, Vol. 46, No. 2, 2004, pp. 329–345.
https://doi.org/10.1137/S0036144503429121

[22] Harrington, R. F., *Field Computation by Moment Methods*, Wiley–IEEE Press, Hoboken, NJ, 1993, Chaps. 1, 2.

[23] Hughes, J. A., and Schaub, H., "Heterogeneous Surface Multisphere Models Using Method of Moments Foundations," *Journal of Spacecraft and Rockets*, Vol. 56, No. 4, 2019, pp. 1259–1266.
https://doi.org/10.2514/1.A34434

[24] Stevenson, D., and Schaub, H., "Multi-Sphere Method for Modeling Electrostatic Forces and Torques," *Advances in Space Research*, Vol. 51, No. 1, 2013, pp. 10–20.
https://doi.org/10.1016/j.asr.2012.08.014

[25] Stevenson, D., and Schaub, H., "Optimization of Sphere Population for Electrostatic Multi-Sphere Method," *IEEE Transactions on Plasma Science*, Vol. 41, No. 12, 2013, pp. 3526–3535.
https://doi.org/10.1109/TPS.2013.2283716

[26] Chung, M., and Everhart, T., "Simple Calculation of Energy Distribution of Low-Energy Secondary Electrons Emitted from Metals Under Electron Bombardment," *Journal of Applied Physics*, Vol. 45, No. 2, 1974, pp. 707–709.
https://doi.org/10.1063/1.1663306

[27] Boris, J. P., "Relativistic Plasma Simulation-Optimization of a Hybrid Code," *Proceedings of the Fourth Conference on Numerical Simulations of Plasmas*, Naval Research Lab., Washington, D.C., 1970, pp. 3–67.

[28] Qin, H., Zhang, S., Xiao, J., Liu, J., Sun, Y., and Tang, W. M., "Why Is Boris Algorithm so Good?" *Physics of Plasmas*, Vol. 20, No. 8, 2013, Paper 084503.
https://doi.org/10.1063/1.4818428

A. D. Ketsdever
Associate Editor

This article has been cited by:

1. Álvaro Romero-Calvo, Gabriel Cano-Gómez, Hanspeter Schaub. Simulation and Uncertainty Quantification of Electron Beams in Active Spacecraft Charging Scenarios. *Journal of Spacecraft and Rockets*, ahead of print1-12. [Abstract] [Full Text] [PDF] [PDF Plus]